RESEARCH ARTICLE OPEN ACCESS

A Custom Deep Learning Model With Explainable Artificial Intelligence for Interpretable Brain Tumor Classification

Duppala Rohan[1] | Boddepalli Yaswanth[1] | V. S. Sai Vardhan[1] | G. Pradeep Reddy[2] | K. Purna Prakash[3] | Y. V. Pavan Kumar[4]

[1]School of Computer Science and Engineering, VIT-AP University, Amaravati, Andhra Pradesh, India | [2]Manipal Institute of Technology, Manipal Academy of Higher Education, Manipal, Karnataka, India | [3]Department of Computer Science and Engineering, Siddhartha Academy of Higher Education, Deemed To Be University, Vijayawada, Andhra Pradesh, India | [4]School of Electronics Engineering, VIT-AP University, Amaravati, Andhra Pradesh, India

Correspondence: Y. V. Pavan Kumar (pavankumar.yv@vitap.ac.in)

ABSTRACT

Brain tumors are critical neurological disorders affecting mankind. The Magnetic Resonance Imaging (MRI) and Computed Tomography (CT) scans play an important role in diagnosing brain tumors, but need an expert interpretation. Although deep learning methods can automate tumor detection, their lack of interpretability and clinical trust remains a major limitation. To address this concern, this paper presents a BrainTumorClassificationNetwork-Convolutional Neural Network (BTCNet-CNN) model with several layers for detecting and classifying MRI scanned images into four categories: glioma, meningioma, no tumor, and pituitary. The model was trained and evaluated on a publicly available dataset comprising 5824 MRI images. Augmentation techniques such as horizontal flipping, random rotations, zooming, shifting, and shearing were implemented on the training set, increasing data diversity and enhancing BTCNet-CNN's robustness to variations in tumor orientation, scale, and position. To evaluate the effectiveness of the proposed model, various popular pre-trained networks such as ResNet50 and InceptionV3 are also implemented on the dataset with metrics such as accuracy, loss, precision, recall, F1 score, and AUROC. Among these three models, the BTCNet-CNN has achieved superior performance with an accuracy of 99.31%, a loss of 0.118, and an average precision, recall, and F1 score of 99.25%, 99.25%, and 99.5%, respectively, on the unseen data. Statistical significance was evaluated using McNemar's test, confirming that BTCNet-CNN's predictions are significantly better than those of ResNet50 and InceptionV3 ($p < 0.05$). To enhance trust and interpretability of models' decisions, various Explainable AI (XAI) techniques, including Occlusion Sensitivity, LIME, Smooth Gradients, and Saliency Maps, were integrated. Finally, a Streamlit-based web application was developed to facilitate real-time prediction and visualization, ensuring practical applicability in clinical diagnosis.

1 | Introduction

A Brain Tumor (BT) occurs due to the unwanted cell division within the brain or its surroundings, leading to disruptions in normal brain function. BT can be classified as non-cancerous or benign and cancerous or malignant. Benign tumors normally grow slowly and are less aggressive, whereas malignant tumors, such as glioblastomas, are extremely dangerous and grow rapidly, and these are often fatal if not treated early [1]. BT can be classified based on its origin and the cells involved within the central nervous system (CNS). Common types include glioma, meningioma, and pituitary adenomas. Gliomas originate from the glial

cells, which support neurons in the brain. Its subtypes include astrocytomas, oligodendrogliomas, and glioblastomas. Glioma can sometimes be slow-growing or aggressive. Glioma commonly occurs in the cerebrum but can occur anywhere in the CNS. Glioblastoma multiforme is one of the most deadly and aggressive forms of glioma. Meningioma arises in the meninges, a protective membrane surrounding the brain and the spinal cord. It's usually benign and slow-growing, but rarely can also be malignant. Meningioma is asymptomatic at first and can cause pressure-related symptoms as it grows. Pituitary adenomas occur in the pituitary gland, which regulates hormones. Though it's typically benign, it affects hormone production. Pituitary adenomas can be classified into two types: functioning adenomas, where hormones are secreted heavily, and non-functioning adenomas, where hormones are not secreted. Pituitary adenomas result in vision problems, hormonal imbalances, and headaches.

Traditional BT diagnosis methods, such as MRI, Computed Tomography (CT) scans, biopsy, and clinical evaluation, rely heavily on radiologists' expertise, which can lead to subjective interpretations, delayed results, and increased diagnostic costs. There is a chance of misinterpretation in early-stage tumors, leading to diagnostic accuracy challenges. Recent advancements in artificial intelligence (AI) are transforming several industries through decision-making, automating procedures, and improving productivity. AI-powered systems are being adopted largely for analyzing medical data and patient monitoring [2–5].

Despite the significant advancements achieved by recent studies in brain tumor detection using deep learning and XAI, several gaps and challenges remain unaddressed. The use of the existing methods is limited to resource-constrained medical settings because they rely on strong designs like DenseNet121, ConvNext, or Vision Transformers, which provide high accuracy at the expense of computing power. Further, several existing studies rely on relatively small or imbalanced datasets, leading to potential overfitting and reduced generalization to unseen clinical data. Moreover, the majority of existing works focus on binary classification tasks, thereby overlooking the need for multi-class brain tumor categorization that is essential for real-world diagnosis.

Another key limitation in prior works is the absence of statistical validation to confirm the significance of model performance. Most studies rely solely on metrics such as accuracy, precision, and F1-score without employing statistical tests to assess comparative effectiveness. Additionally, while XAI methods have improved visual transparency, limited research explores how such interpretability translates into clinician trust and adoption in real diagnostic workflows. This study introduces the BTCNet-CNN model, which aims to provide a computationally efficient, interpretable, and statistically validated framework for multi-class brain tumor classification. The model also enhances clinical trust through XAI-based visualization and facilitates real-time interaction via a Streamlit-based web application.

The following are the research objectives:

- To design and build a deep learning model for classifying BT from MRI scans precisely and accurately.

- To integrate XAI techniques such as Occlusion Sensitivity, LIME, Smooth Gradients, and Saliency Maps to improve trust and transparency in the models' decisions.

- To develop a web interface using Streamlit that enables real-time BT prediction and provides visual explanations.

The novelty of this work lies in the design and implementation of a lightweight, highly accurate deep learning model tailored for multi-class brain tumor classification from MRI images. Unlike conventional architectures that are computationally heavy or limited to binary classifications, BTCNet-CNN achieves greater accuracy with less complexity through an optimized convolutional block structure and data augmentation. Furthermore, the use of multiple XAI techniques such as Occlusion Sensitivity, LIME, Smooth Gradients, and Saliency Maps ensures that the model's decision-making process is interpretable and transparent, addressing one of the most significant barriers to the clinical adoption of AI. Another distinguishing feature of this work is the statistical validation using McNemar's test, which rigorously confirms that the reported performance of BTCNet-CNN over existing state-of-the-art models such as ResNet50 and InceptionV3 is statistically significant. Finally, a Streamlit-based web interface has been developed to facilitate real-time interaction and visualization, bridging the gap between research and practical clinical application.

The rest of the paper is organized as follows: a thorough analysis of existing literature on BT detection is presented in Section 2. The methodology and architecture of the proposed BTCNet-CNN model are detailed in Section 3. Section 4 presents the experimental results, followed by Section 5, which offers discussion and insights into the findings. Section 6 describes the Streamlit hosting implementation for real-time deployment, and finally, Section 7 concludes the paper with a summary of key findings and directions for future work.

2 | Related Works

Recently, DL and ML models have gained significant attention for improving brain tumor classification and diagnosis. The increasing demand for transparency and reliability in medical decision-making has driven researchers to explore interpretable frameworks that not only enhance classification performance but also address the black-box nature of conventional systems [6–8]. Table 1 outlines recent studies focusing on BT detection and classification, highlighting the role of explainability in improving model interpretability and clinical trust. These studies show that XAI with DL models is a promising way to build systems that are not only accurate but also easy to understand and trust. Adding XAI techniques is an important step toward using DL systems more effectively in real-world clinical settings for BT diagnosis.

3 | Description of the Proposed Method

This section outlines the dataset and the data augmentation techniques. It also discusses the custom BTCNet-CNN architecture along with ResNet50 and InceptionV3 through transfer learning.

TABLE 1 | Summary of recent studies on BT diagnosis.

Refs.	Year	Objective	Approach	Relevance
[9]	2025	To develop a lightweight and powerful segmentation framework that reduces computational overhead while maximizing detection performance.	Introduces a deep learning model combining a U-Net architecture with EfficientNetB4 for feature extraction.	Accurate BT segmentation enhances medical decision-making and treatment outcomes, improving early diagnosis.
[10]	2025	To develop a CNN framework based on DenseNet121 to accurately detect and classify BT from MRI scans, while ensuring diagnostic transparency using XAI techniques.	Utilizes a DenseNet121-derived CNN model enhanced with Grad-CAM++ visualization to achieve precise identification of various BT types.	Addresses key challenges in neuro-oncology, enhances trust in AI-assisted clinical workflows, and supports healthcare professionals in delivering reliable BT diagnoses.
[11]	2025	To propose a federated learning method for the BT detection using MRI data, enhancing the transparency and trustworthiness.	Employs visualization techniques like heatmaps and Grad-CAM to explain model predictions and ensures data security through federated learning.	Addresses the need for accurate and explainable BT classification by employing XAI techniques within a privacy-preserving federated learning framework.
[12]	2025	To enhance the diagnosis of BT by developing a new detection framework that utilizes AI methods and improves MRI image quality through preprocessing methods.	Integrates a CLAHE method for image enhancement, employing data augmentation techniques.	Improves the speed of BT detection and aims to improve patient outcomes by facilitating early diagnosis and treatment.
[13]	2025	To develop a Deep Siamese CNN (DeepSCNN) model for optimal BT classification and diagnosis using MRI scans	Employed 3064 contrast-enhanced T1-weighted brain MRI images and utilized five advanced classification models, including DeepSCNNs, evaluating performance through accuracy, precision, sensitivity, recall, and F1-score.	Demonstrates that accurate and timely BT classification using DeepSCNNs can significantly enhance diagnostic precision and inform better treatment strategies in neuro-oncology.
[14]	2025	To develop a hybrid deep learning model that enhances brain tumor classification accuracy by fusing features from multiple pre-trained CNN architectures.	The model integrates VGG16, ResNet50, and MobileNetV2 through transfer learning and fine-tuning, combining their extracted features for robust classification across four public datasets.	Addresses limitations in existing models by improving diagnostic precision across diverse MRI datasets, supporting more reliable computer-aided clinical decisions.
[15]	2024	To build a deep learning model that integrates CNN and GNN architectures for more accurate brain tumor classification using MRI images.	The model fuses spatial features from CNNs with contextual relationships captured by GNNs, trained on a large, balanced dataset of MRI scans to improve classification performance.	Addresses limitations of traditional CNN-based models by incorporating graph-based relational analysis, enhancing diagnostic precision in complex medical imaging.
[16]	2024	To develop a deep hybrid model that fuses DenseNet169 with machine learning classifiers for accurate classification of brain tumors from MRI images.	The model extracts features using DenseNet169 and applies SVM, Random Forest, and XGBoost combined via majority voting to improve classification performance on the Figshare dataset.	Addresses challenges in medical image classification, especially with limited data, by enhancing diagnostic precision through ensemble learning and transfer learning techniques.
[17]	2024	To implement a deep learning model for accurate BT detection while incorporating XAI techniques to improve clinical trust.	Trained on the BR35H dataset containing 3060 MRI images and utilizes LIME, SHAP, and Grad-CAM for interpreting CNN predictions, achieving 98.67% accuracy on the unseen data.	Significantly improve the early BT detection, which is essential for patient survival and treatment outcomes.

(Continues)

TABLE 1 | (Continued)

Refs.	Year	Objective	Approach	Relevance
[18]	2024	To develop a BT classification technique using the ConvNext architecture, which processes MRI data for accurate diagnosis and treatment planning.	Used ConvNext-based CNN architecture with transfer learning to extract MRI features, then classified using a fully connected neural network, effectively addressing data scarcity in medical imaging.	Enhances non-invasive BT diagnosis by offering an efficient classification using modern CNN architectures, improving treatment planning, patient outcomes, and solving computational challenges in medical imaging.
[19]	2024	To improve the precision and effectiveness of BT detection, addressing the challenges posed by various tumor types and their spatial positioning.	Adapts the VGG19 architecture with an Inverted Pyramid Pooling Module from MRI images and employs LIME for model interpretability in classifying four BT types.	Advances in early and accurate classification of BT by addressing dataset imbalance and tumor variability, thereby supporting improved diagnosis and treatment outcomes in neuro-oncology.
[20]	2024	To implement a TransXAI model for explainable and precise segmentation of gliomas and their sub-regions in multimodal brain MRI scans by generating surgeon-understandable heatmaps to increase the transparency.	Integrates CNNs for extracting local features and a Vision Transformer (ViT) for modeling long-range dependencies, with Grad-CAM employed as a post hoc XAI technique to generate visual heatmaps.	Addresses the critical need for XAI in medical imaging, particularly for glioma segmentation, increasing the trust and acceptance of deep learning systems among medical professionals.
[21]	2023	To develop an explainable deep learning framework for MRI-based BT analysis. This supports clinical decision-making by providing interpretable classification outcomes using able deep models.	Employs a composite network combining a 3D nnU-Net for tumor segmentation and a re-parameterized classification model to distinguish between high-grade and low-grade gliomas.	Enhances transparency and trust, addressing the ethical and regulatory demands for XAI in healthcare, and aiding clinicians in making accurate decisions.

Training and evaluating the models is discussed, followed by the XAI techniques utilized.

3.1 | Dataset Description

The dataset [22] consists of 5824 MRI-scanned brain images, classified into four classes. The dataset was already split in an 80:10:10 ratio into training, validation, and testing sets. There are 1168 images in each class, for a total of 4672 images in the training set. Each class in the testing and validation sets has 144 images, for a total of 576 images. Figure 1 depicts the sample images from each class of the training set.

3.2 | Data Augmentation

Data Augmentation was applied to the training set to reduce the chances of overfitting and to simulate real-world variations, and to improve the models' generalization power. A combination of geometric and photometric transformations was applied to the training dataset, including random horizontal flipping, small random rotations, zooming, shifts, and shearing. For the testing and validation datasets, only rescaling was used, ensuring consistent model evaluation without introducing artificial variation.

The specific data augmentation parameters used are presented in Table 2.

3.3 | BTCNET-CNN

As seen in Figure 2, BTCNet-CNN comprises four convolutional blocks followed by fully connected layers. Each convolutional block contains two convolutional layers, maintaining spatial resolution through same-padding. After every pair of convolutions, a max pooling layer reduces the spatial dimensions, followed by batch normalization to stabilize and accelerate training. The filter size increases progressively from 64 in the first block to 512 in the fourth block, allowing the network to learn complex features at deeper levels. Following the convolutional layers, the feature maps are flattened and passed through two dense layers with 512 and 256 neurons, respectively, each followed by dropout layers with dropout rates of 0.4 and 0.3 to mitigate overfitting. Both dense layers employ L2 regularization to enhance generalization. Finally, a softmax-activated output layer of four units corresponds to the four target tumor types.

Let the input image be:

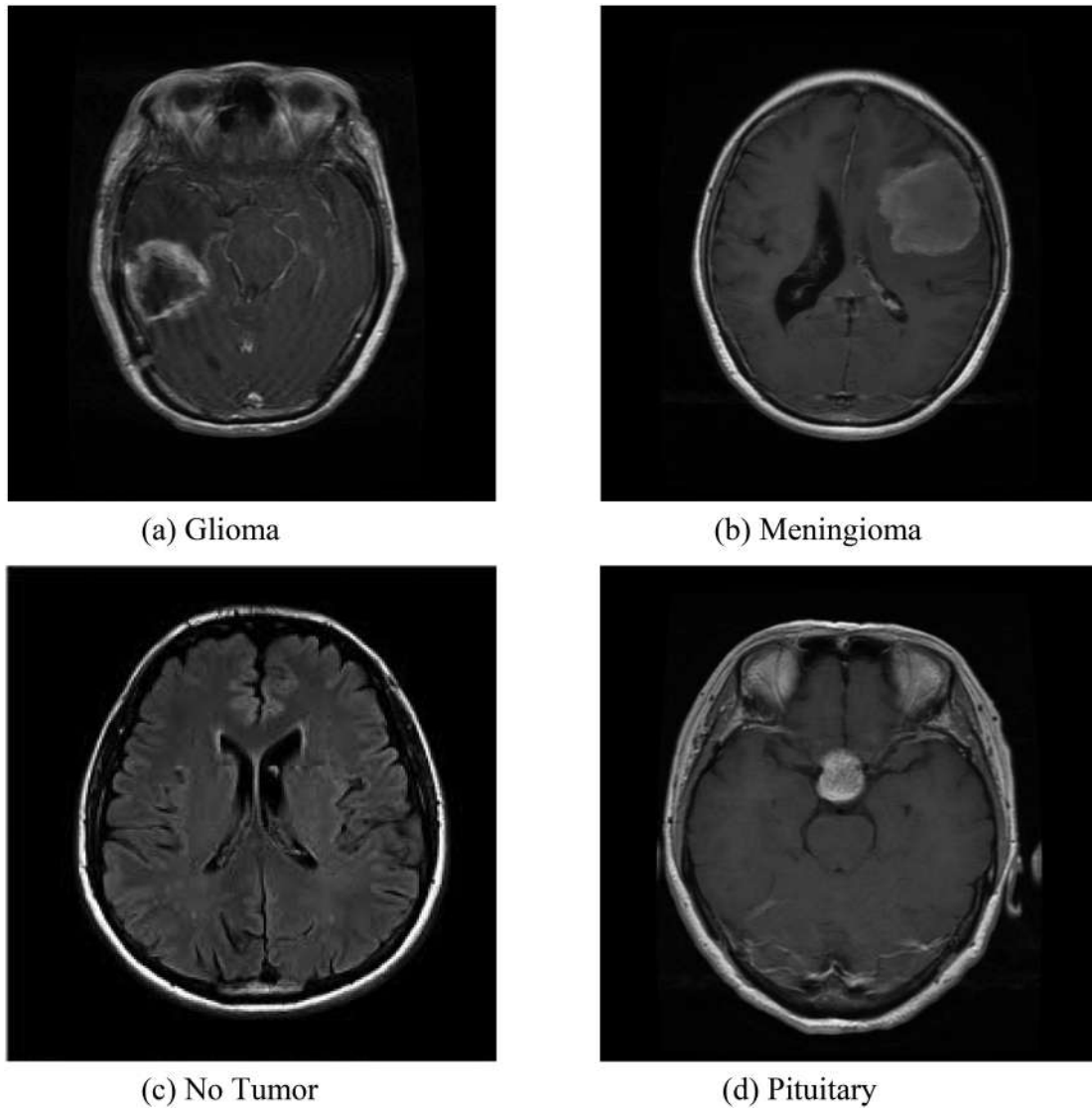$$X \in \mathbb{R}^{224 \times 224 \times 3}$$

(a) Glioma

(b) Meningioma

(c) No Tumor

(d) Pituitary

FIGURE 1 | Training dataset images from each class.

TABLE 2 | Data augmentation parameters.

Augmentation technique	Value
Rotation Range	10°
Width Shift Range	0.1
Height Shift Range	0.1
Shear Range	0.1
Zoom Range	0.1
Horizontal Flip	True

Each convolutional layer with ReLU activation is:

$$F^{(l)} = ReLU\left(W^{(l)} * F^{(l-1)} + b^{(l)}\right), l = 1, 2, 3, \ldots, 8$$

where $F^{(0)}$ indicates X, $*$ indicates 2D convolution, and $W^{(l)}$, $b^{(l)}$ are weights and biases. The blocks are organized as:

- Block 1 (64 filters): $l = 1$, 2
- Block 2 (128 filters): $l = 3$, 4

- Block 3 (256 filters): $l = 5$, 6
- Block 4 (512 filters): $l = 7$, 8

After each block of two convolutions, max-pooling was applied:

$$F_{pooled}^{(b)} = MaxPool\left(F^{(l)}, k = 2, s = 2\right)$$

Followed by batch normalization:

$$\widehat{F}^{(b)} = \gamma \frac{F_{pooled}^{(b)} - \mu}{\sqrt{\sigma^2 + \epsilon}} + \beta$$

where k, s denotes kernel size, μ, σ^2 are batch statistics, and γ, β are learnable parameters.

The resulting feature map is flattened:
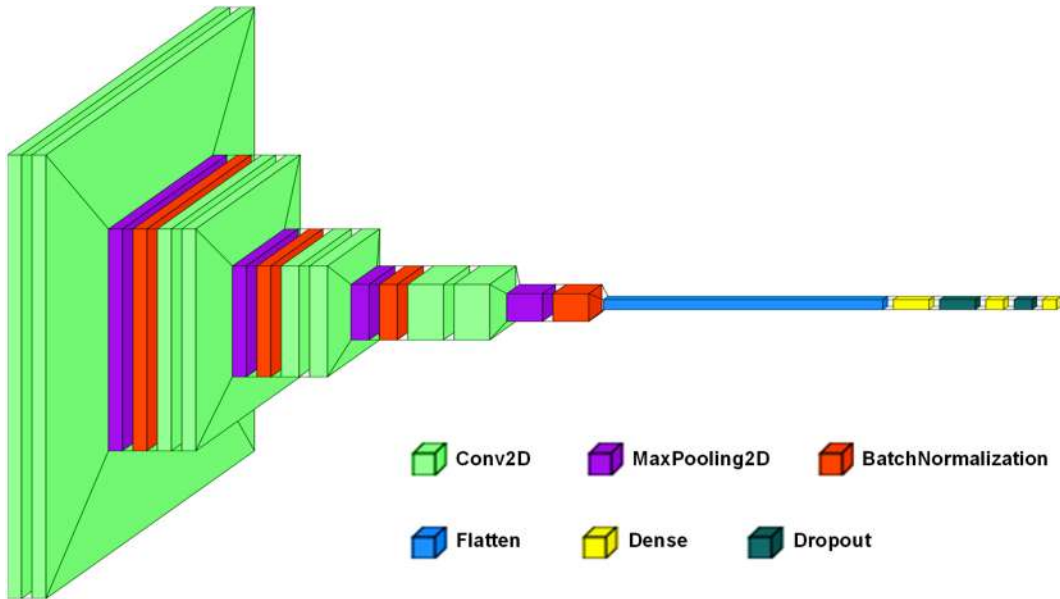
$$f = Flatten\left(\widehat{F}^{(4)}\right)$$

FIGURE 2 | Architecture of BTCNet-CNN.

And passed through two fully connected dense layers with ReLU, L2 regularization, and dropout:

$$h^{(1)} = ReLU\big(W^{(1)}f + b^{(1)}\big) + \lambda\big\|W^{(1)}\big\|_2^2$$

$$h^{(1)}_{drop} = Dropout\big(h^{(1)}, p = 0.4\big)$$

$$h^{(2)} = ReLU\Big(W^{(2)}h^{(1)}_{drop} + b^{(2)}\Big) + \lambda\big\|W^{(2)}\big\|_2^2$$

$$h^{(2)}_{drop} = Dropout\big(h^{(2)}, p = 0.3\big)$$

The softmax output layer generates class probabilities:

$$\hat{y} = softmax(z), z = W^{(out)}h^{(2)}_{drop} + b^{(out)}$$

Or equivalently, for each class $i = 1, 2, 3, 4$:

$$\hat{y}_i = \frac{e^{z_i}}{\sum_{j=1}^4 e^{z_j}}$$

where $h^{(2)}_{drop}$ is the output of the last dense layer after dropout, $W^{(out)}$ and $b^{(out)}$ are the output layer's weights and biases, and $\hat{y}_i$ is the predicted probability of class i, with $\sum_{i=1}^4 \hat{y}_i = 1$.

The overall network can be expressed as a composition of operations:

$$\hat{y} = Softmax \circ Dropout_2 \circ FC_2 \circ Dropout_1 \circ FC_1 \circ Flatten$$

$$\circ \prod_{b=1}^4 \big(Batch\ Normalization \circ MaxPool \circ Conv_2 \circ Conv_1\big)(X)$$

3.4 | Transfer Learning

In addition to BTCNet-CNN, transfer learning was employed using ResNet50 and InceptionV3, as shown in Figure 3. Fine-tuning was done to leverage the rich feature representations learned from large-scale image datasets such as ImageNet.

ResNet50 was chosen because of its ability to minimize the vanishing gradient problem using residual connections, enabling training without degradation in performance. InceptionV3, on the other hand, was selected for its efficient utilization of computational resources and its architectural strength in capturing multi-scale spatial features via inception modules.

3.5 | Training and Evaluation

EarlyStopping, ModelCheckpoint, and ReduceLROnPlateau callback mechanisms were included to avoid overfitting and ensure generalization. For BTCNet-CNN, the early stopping was set to 10 epochs. The model with the lowest validation loss was maintained during training by using ModelCheckpoint to save the optimal model weights. When the validation loss reaches a plateau, the ReduceLROnPlateau callback lowers the learning rate, enabling the model to adjust the weights in later epochs. BTCNet-CNN used a learning rate reduction patience of 5 epochs. BTCNet-CNN's training started at a learning rate of 0.000001. The maximum epochs set for BTCNet-CNN's training was 200, considering its larger capacity and the need for a longer training window to capture feature representations. The training configuration parameters are listed in Table 3. Accuracy, loss, precision, recall, F1 score, and AUROC were considered for evaluating the models.

3.6 | XAI Techniques

This sub-section presents the XAI integration into the experiment. Four techniques were adopted, namely, Occlusion Sensitivity, LIME, Smooth Gradients, and Saliency Maps. These techniques were employed to generate visual explanations that improve transparency in the models' decisions.

3.6.1 | Occlusion Sensitivity

Occlusion sensitivity [23] systematically occludes parts of the input image and observes the influence on the prediction
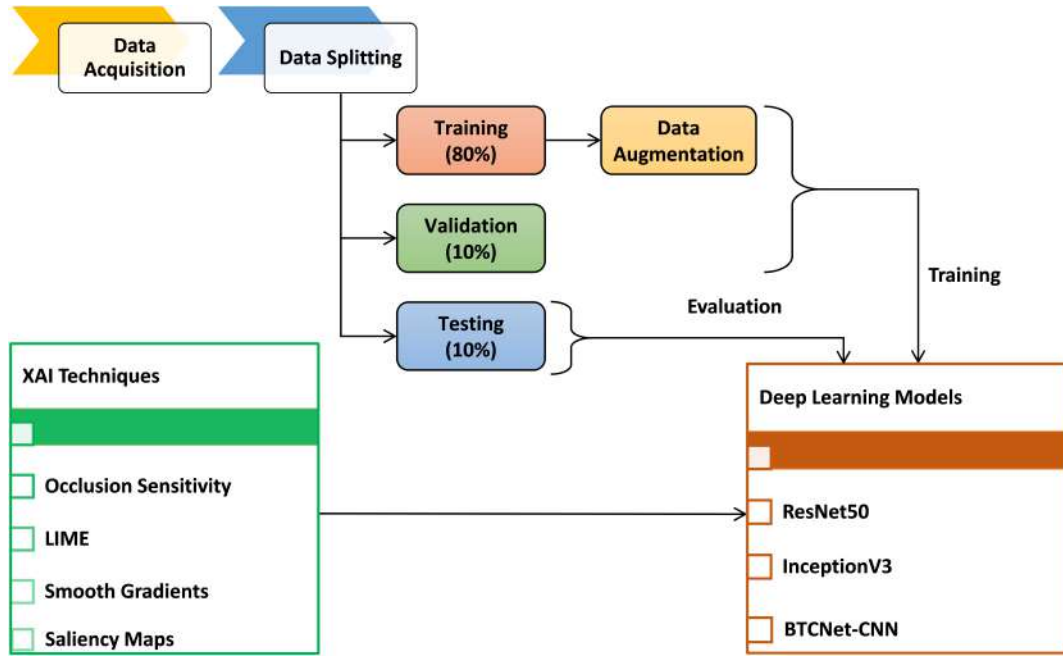
FIGURE 3 | Experimental workflow.

TABLE 3 | Training configuration of BTCNet-CNN.

Training parameter	Values
Initial Learning Rate	1×10^{-6}
Epochs	200
Optimizer	Adam
Loss Function	Categorical Cross-Entropy
Early Stopping Patience	10
ReduceLROnPlateau Patience	5
ReduceLROnPlateau Factor	0.5
Minimum Learning Rate	1×10^{-6}

probability. This helps to discover relevant regions that influence the model's choice. First, it divides the image into overlapping or non-overlapping patches. Then, each patch is replaced with a baseline value (e.g., black or the mean pixel value). Finally, the change in prediction probability for the target class is computed.

Let: $x \in R^{H \times W \times C}$: Input image. $f_c(x)$: Output probability for class c. $M_{i,j}$: Occlusion mask centered at (i, j) of size k×k. $x_{i,j} = x \odot (1 - M_{i,j}) + v \cdot M_{i,j}$, where v is the baseline pixel value. Then,

$$\Delta f_c(i,j) = f_c(x) - f_c(x_{i,j}) \tag{1}$$

Equation (1) gives a heatmap showing the importance of region (i, j) for class c.

3.6.2 | LIME

By varying the input and monitoring changes in the output, LIME [24] provides a local approximation of the model using an interpretable linear model. The input image is perturbed by turning off super pixels. The black-box model is used to get predictions for perturbed inputs. A linear model is fitted on these samples, weighted by proximity to the original input. Equation (2) represents the objective function of LIME.

Let: f: Black-box model. x: Original input. z: Binary vector indicating presence/absence of super pixels. $g(z) = w^T z$: Interpretable linear model. $\pi_x(z)$: Proximity measure (e.g., exponential kernel). Then the objective is:

$$\underset{w \in R^d}{argmin} L(f, g, \pi_x) + \Omega(g) \tag{2}$$

where L: Loss function; $\Omega(g)$: Regularizer to keep g simple (e.g., sparsity constraint).

3.6.3 | Smooth Gradients

Smooth Gradients [25] reduces noise in gradient-based saliency maps by averaging gradients over noisy input samples. A total of noisy versions of the input image are generated by adding Gaussian noise. Compute gradients for each noisy version of the input image and average them. This results in a less noisy and more robust saliency map. Equation (3) represents the mathematical formulation of the Smooth Gradients.

Let: $f_c(x)$: Score for class c. $\nabla_x f_c(x)$: Gradient of the score to input. $\mathcal{N}(0, \sigma^2)$: Gaussian noise.

$$\text{SmoothGrad}(x) = \frac{1}{n} \sum_{i=1}^{n} \nabla_x f_c(x + N_i) \tag{3}$$

3.6.4 | Saliency Maps

Saliency Maps [26] highlight input pixels with the biggest impact on the model's prediction by computing the output's gradient to

the input. Firstly, the class score gradient for the image is computed. Then the absolute value or maximum channel-wise gradient is visualized as a heatmap, as shown in Equation (4).

Let: x: Input image. $f_c(x)$: Gradient of class score. $S_c(x) = \frac{\partial f_c(x)}{\partial x}$: Class score gradient of the input image.

$$Saliency(x) = \max_c \left| \frac{\partial f_c(x)}{\partial x} \right| \qquad (4)$$

4 | Experimental Results

ResNet50 achieved a validation and testing accuracy of 77.08% and 74.65%, respectively. The performance drop between the training and testing stages suggests that ResNet50 struggled to generalize well to unseen data. The class-wise performance also reflected this, particularly for the meningioma class, where precision and recall were only 60% and 40%, respectively. InceptionV3 exhibited better performance, with a training accuracy of 96.81% and a testing accuracy of 92.01%, as shown in Table 4. This model leveraged inception modules to extract multi-scale features, which proved advantageous for classifying heterogeneous tumor types. However, while it performed well overall, some inconsistencies were still observed, such as a relatively lower recall of 91% for the pituitary class, as shown in Table 5.

BTCNet-CNN outperformed across all metrics by achieving training, validation, and testing accuracy of 99.85%, 94.1%, and 99.31%, respectively, demonstrating both effective learning and robust generalization. The testing loss was the lowest among all models at 0.118, indicating high confidence in its predictions. Furthermore, the BTCNet-CNN achieved high precision, recall, and F1-scores, with 100% F1-scores for glioma and pituitary, and 99% for meningioma and no tumor.

ResNet50 model exhibited inconsistent class-level performance, with an AUROC of 0.9642 for glioma, 0.7477 for meningioma, 0.9433 for no tumor, and 0.9836 for pituitary, as shown in

Figure 4a. While the AUROC for most classes was relatively high, the low AUROC for meningioma reflected its weak predictive performance, also evident in the confusion matrix. Figure 4b showed significant misclassifications, particularly between meningioma and no tumor, where 64 non-tumor samples were misclassified as meningioma, and 57 meningioma samples were misclassified. This suggests ResNet50 struggled with inter-class similarity, particularly between these two categories.

It can be observed from Figure 5a that InceptionV3 displayed improved discriminative ability with AUROC values of 0.9914 for glioma, 0.9741 for meningioma, 0.9888 for no tumor, and 0.9964 for pituitary. The confusion matrix for InceptionV3 confirmed this improvement, showing notably better classification for glioma and pituitary. However, misclassification remained between meningioma and no tumor, with 53 no tumor samples misclassified as meningioma, as shown in Figure 5b.

The BTCNet-CNN achieved high AUROC scores: 1.0 for glioma, 1.0 for no tumor, 1.0 for pituitary, and 0.9996 for meningioma, as shown in Figure 6a. Figure 6b shows ideal classification: all samples for glioma, no tumor, and pituitary were correctly predicted, and only four samples in total were misclassified across all classes (three meningioma samples misclassified as no tumor, and one as pituitary). This near-ideal performance highlights the superior capability of BTCNet-CNN in modeling the subtle features unique to each tumor class.

These results collectively demonstrate that the proposed BTCNet-CNN not only generalizes well to unseen data but also significantly outperforms transfer learning-based models in class-level discrimination, especially for challenging class pairs such as meningioma and no tumor.

4.1 | Statistical Analysis

McNemar's test [27] was employed to evaluate the observed performance of the proposed BTCNet-CNN. This test is specifically

TABLE 4 | Accuracy and loss.

Model	Training accuracy	Training loss	Validation accuracy	Validation loss	Testing accuracy	Testing loss
ResNet50	82.9%	0.472	77.08%	0.508	74.65%	0.653
InceptionV3	96.81%	0.187	81.25%	0.490	92.01%	0.300
BTCNet-CNN	99.85%	0.095	94.1%	0.338	99.31%	0.118

TABLE 5 | Precision, recall, and F1 score.

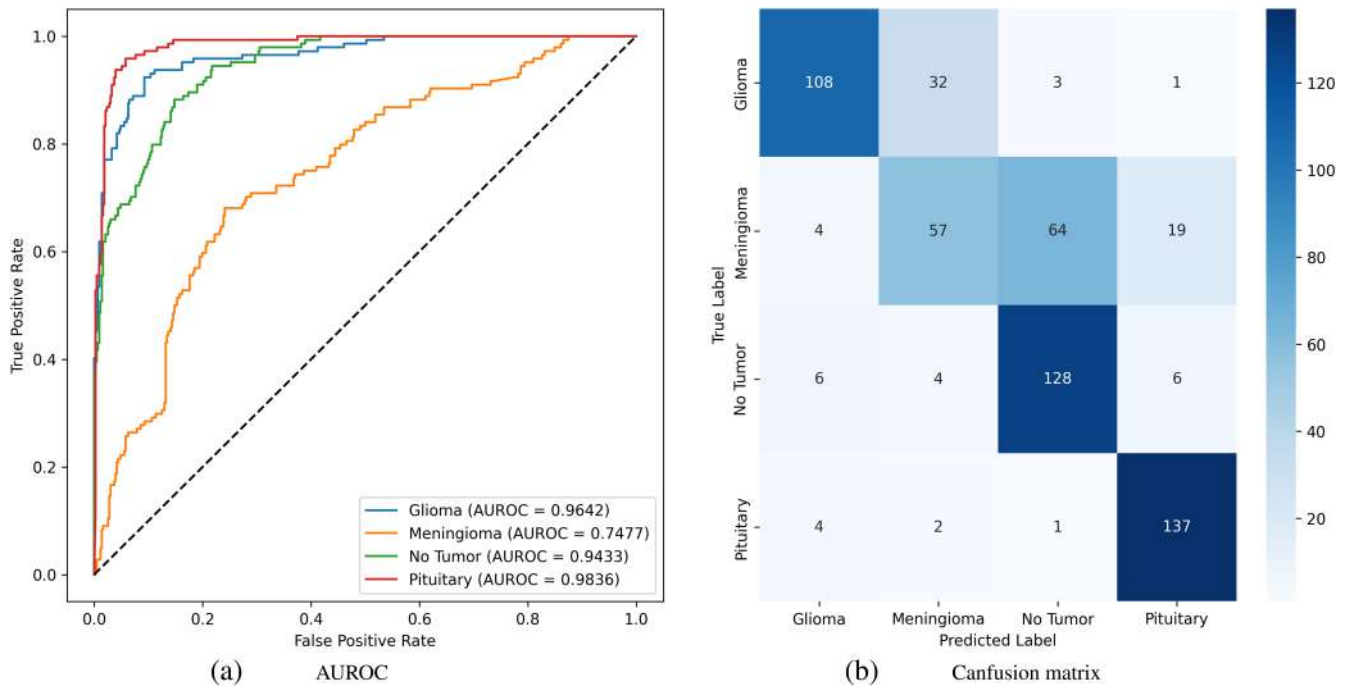|	ResNet50			InceptionV3			BTCNet-CNN		
Class	Precision (%)	Recall (%)	F1 Score (%)	Precision (%)	Recall (%)	F1 Score (%)	Precision (%)	Recall (%)	F1 Score (%)
Glioma	89	75	81	95	88	91	100	100	100
Meningioma	60	40	48	78	96	86	100	97	99
No Tumor	65	89	75	99	94	96	98	100	99
Pituitary	84	95	89	100	91	95	99	100	100

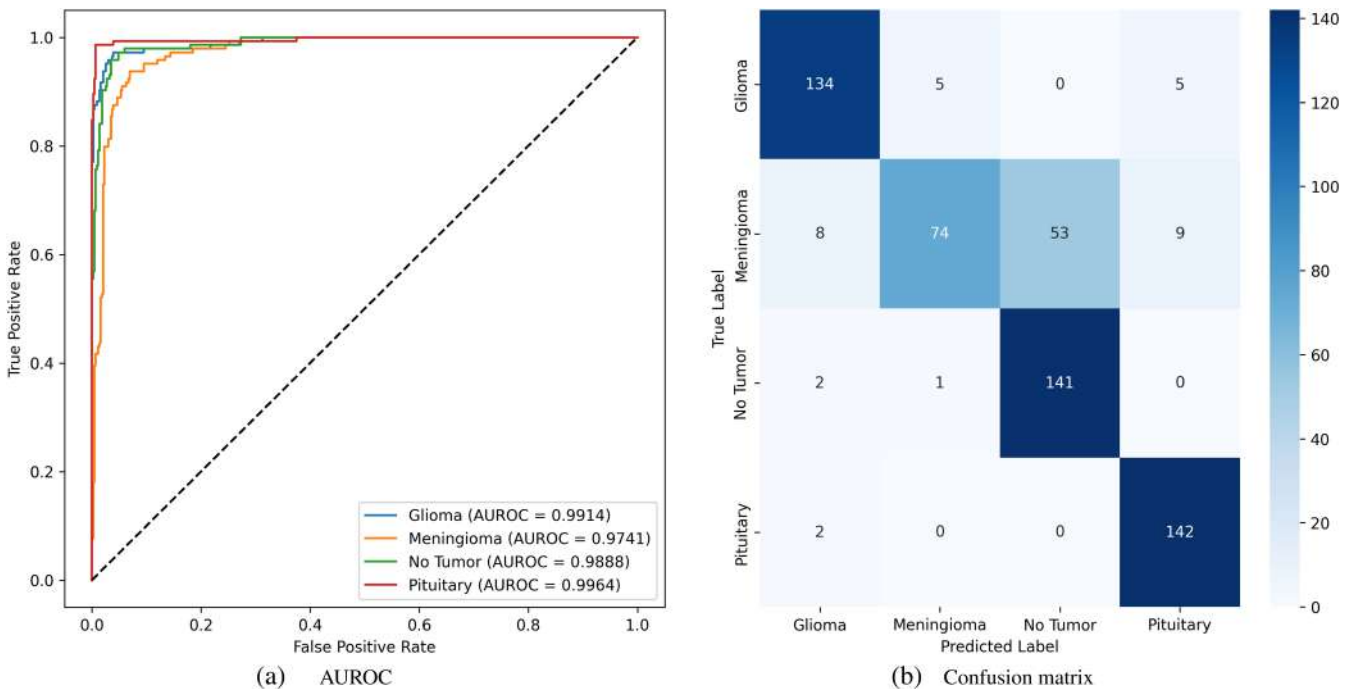**FIGURE 4** | AUROC and confusion matrix of ResNet50.

FIGURE 5 | AUROC and confusion matrix of InceptionV3.

suited for comparing the classification performance of two models on the same test samples and checks whether two models differ significantly in how often they misclassify the same test samples. McNemar's test assesses whether the models differ significantly in the proportion of instances.

Table 6 presents the contingency table comparing BTCNet-CNN with ResNet50. Here, 429 represents the number of instances correctly classified by both models, while 3 indicates the number of instances misclassified by both. The values 143 and 1 are the number of instances correctly classified by BTCNet-CNN but
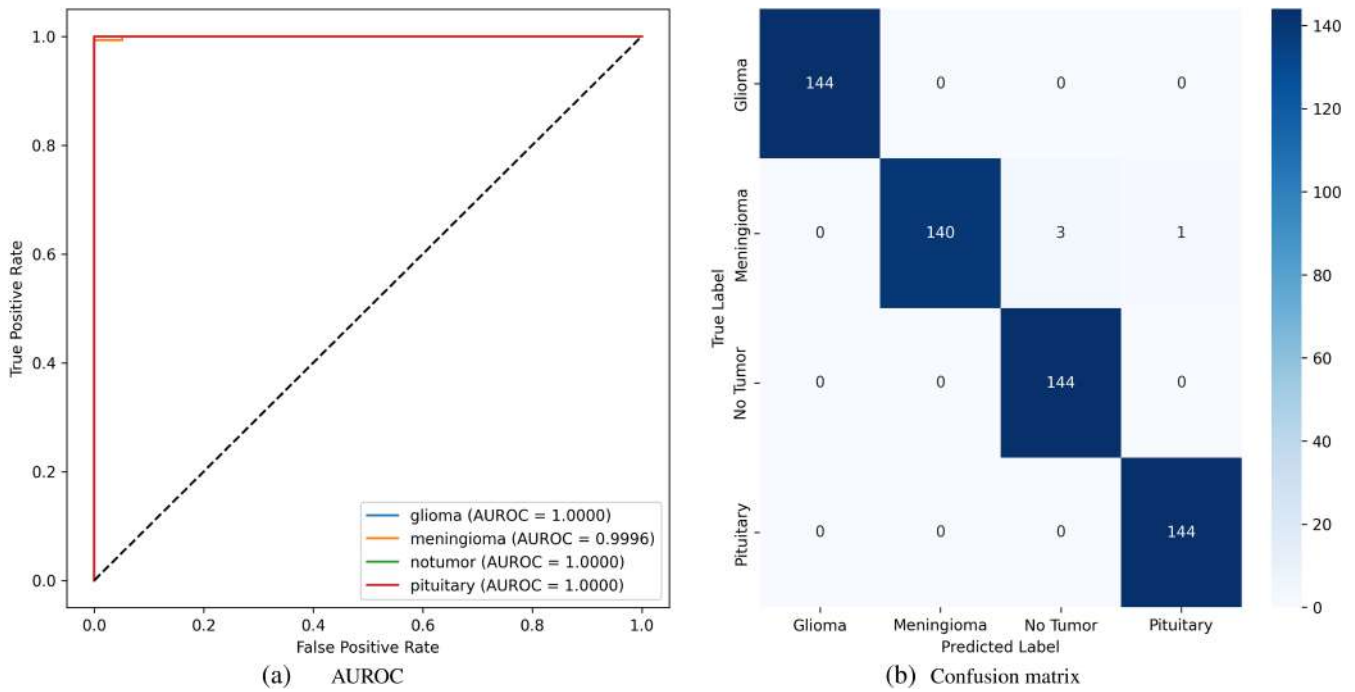
FIGURE 6 | AUROC and confusion matrix of BTCNet-CNN.

TABLE 6 | BTCNet-CNN vs. ResNet50.

	ResNet50 Correct	ResNet50 Wrong
BTCNet-CNN Correct	429	143
BTCNet-CNN Wrong	1	3

TABLE 7 | BTCNet-CNN vs. InceptionV3.

	InceptionV3 Correct	InceptionV3 Wrong
BTCNet-CNN Correct	526	46
BTCNet-CNN Wrong	4	0

TABLE 8 | McNemar's test results.

Comparison	*p*-value	Chi-square
BTCNet-CNN vs. ResNet50	7.06×10^{-34}	138.06
BTCNet-CNN vs. InceptionV3	6.7×10^{-9}	33.62

the comparison between BTCNet-CNN and InceptionV3 produced a chi-square value of 33.62 with a *p*-value of 6.7×10^{-9}, as tabulated in Table 8. Since both *p*-values are far below the conventional significance threshold of 0.05, the results confirm that the superior performance of the proposed BTCNet-CNN model over ResNet50 and InceptionV3 is statistically significant and not attributable to random chance.

4.2 | BTCNET-CNN Interpretation Using XAI Techniques on the Dataset Images

Figure 7 illustrates a representative set of randomly selected brain MRI images drawn from the unseen data, that is, the testing set, which serves as a visual benchmark for evaluating the performance of BTCNet-CNN. To better understand the decision-making behavior of BTCNet-CNN, XAI techniques were systematically applied to these test images. This interpretability analysis plays a crucial role in validating the clinical relevance of the model by highlighting the regions within the brain MRI scans that most strongly influenced the classification outcomes.

Figures 8–11 present the resulting visualizations, where color-coded heatmaps and pixel segmentations mark the
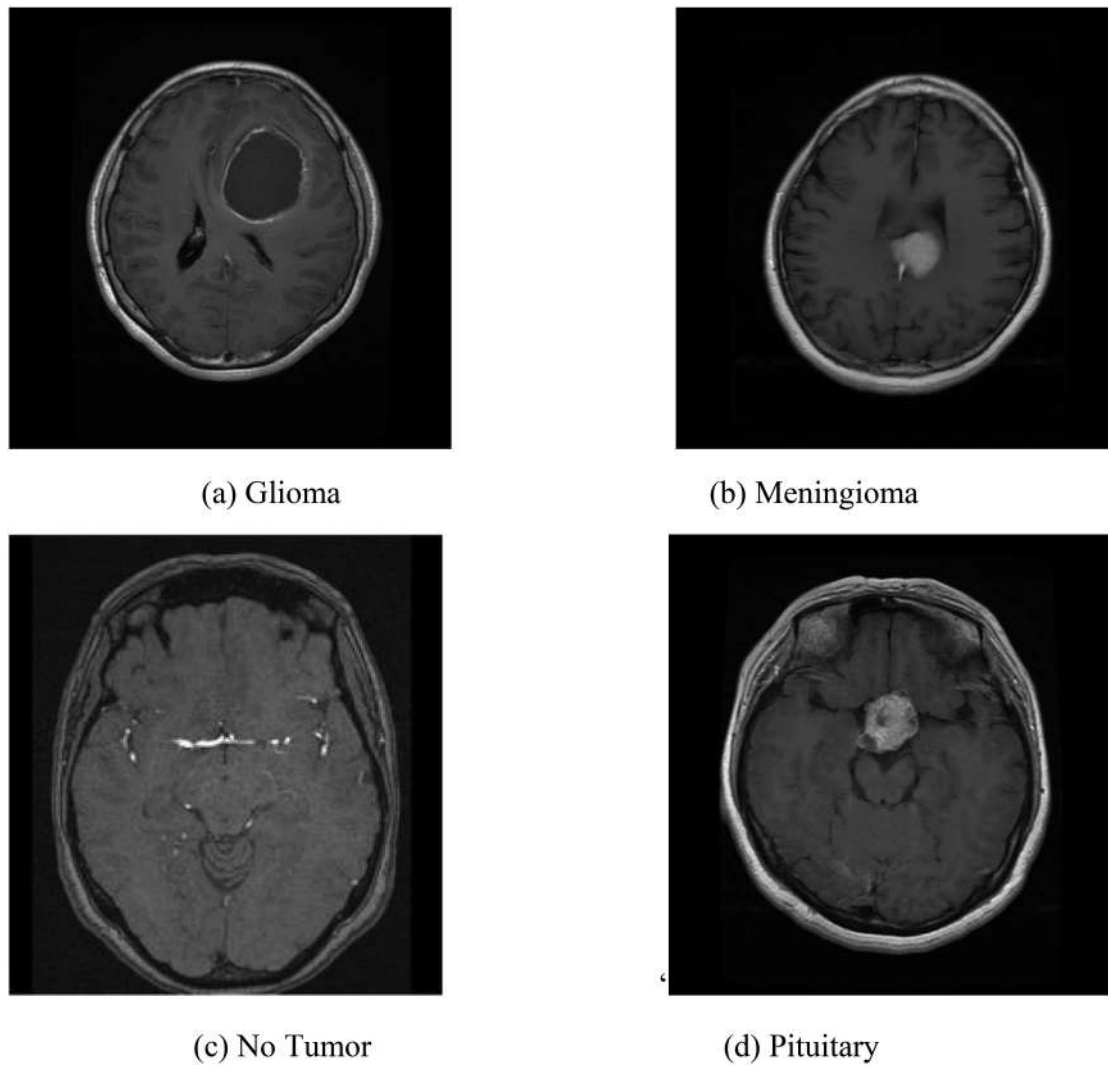
misclassified by ResNet50, and vice versa, respectively. The large difference between 143 and 1 demonstrates that BTCNet-CNN correctly identified significantly more cases than ResNet50 failed to classify accurately.

Table 7 shows the contingency table comparing BTCNet-CNN with InceptionV3. In this case, 526 denotes the number of samples both models classified correctly, whereas 0 shows that there were no instances where both models misclassified the same sample. 46 and 4 represent the instances correctly identified by BTCNet-CNN but missed by InceptionV3, and vice versa. The asymmetry (46 > 4) indicates that BTCNet-CNN achieved better classification performance.

The comparison between BTCNet-CNN and ResNet50 yielded a chi-square value of 138.06 with a *p*-value of 7.06×10^{-34}, while

(a) Glioma

(b) Meningioma

(c) No Tumor

(d) Pituitary

FIGURE 7 | Sample images from the testing set.

areas of focus that guided the model's predictions (indicated with yellow-colored circles). From these figures, the following observations can be made.

From Figures 8a, 9a, 10a, and 11a, occlusion sensitivity demonstrated a strong correlation between tumor regions and the model's prediction confidence for glioma and meningioma cases. By systematically masking small patches of the input image, it was evident that occluding areas near the lesion led to a significant drop in classification confidence, highlighting the model's reliance on pathological features. However, for pituitary tumors, this technique was less effective. Due to their smaller size and proximity to complex anatomical structures, occlusion did not substantially alter the model's confidence, resulting in less informative relevance maps. In contrast, for the no-tumor class, the heatmaps showed widespread red regions, suggesting that BTCNet-CNN adopted a holistic representation for normal scans while focusing locally for pathological ones.

From Figures 8b, 9b, 10b, and 11b, LIME produced highly interpretable superpixel-based visualizations that highlighted the most influential image segments. In tumor-positive cases, LIME distinguished the lesion areas by identifying superpixels that overlapped with tumor boundaries as major contributors to the classification. This not only validates the model's attention to clinically relevant structures but also provides clinicians with interpretable, human-friendly explanations that closely align with visible abnormalities in the MRI scans. For no-tumor cases, LIME detected only minimal and scattered regions, further reinforcing that the absence of lesion-related features led to confident classification decisions.

From Figures 8c, 9c, 10c, and 11c, smooth gradients refined the saliency map approach by averaging gradients over multiple noisy perturbations, producing smoother activation maps. This method effectively highlighted lesion locations in glioma and meningioma images, with concentrated gradient flows that made diseased regions stand out. However, for pituitary tumors, the gradient activations were diffuse and noisy, failing to localize the tumor effectively. This limitation stems from the anatomical complexity and subtle visual features of pituitary tumors, which challenge gradient-based methods. In no-tumor cases, the absence of
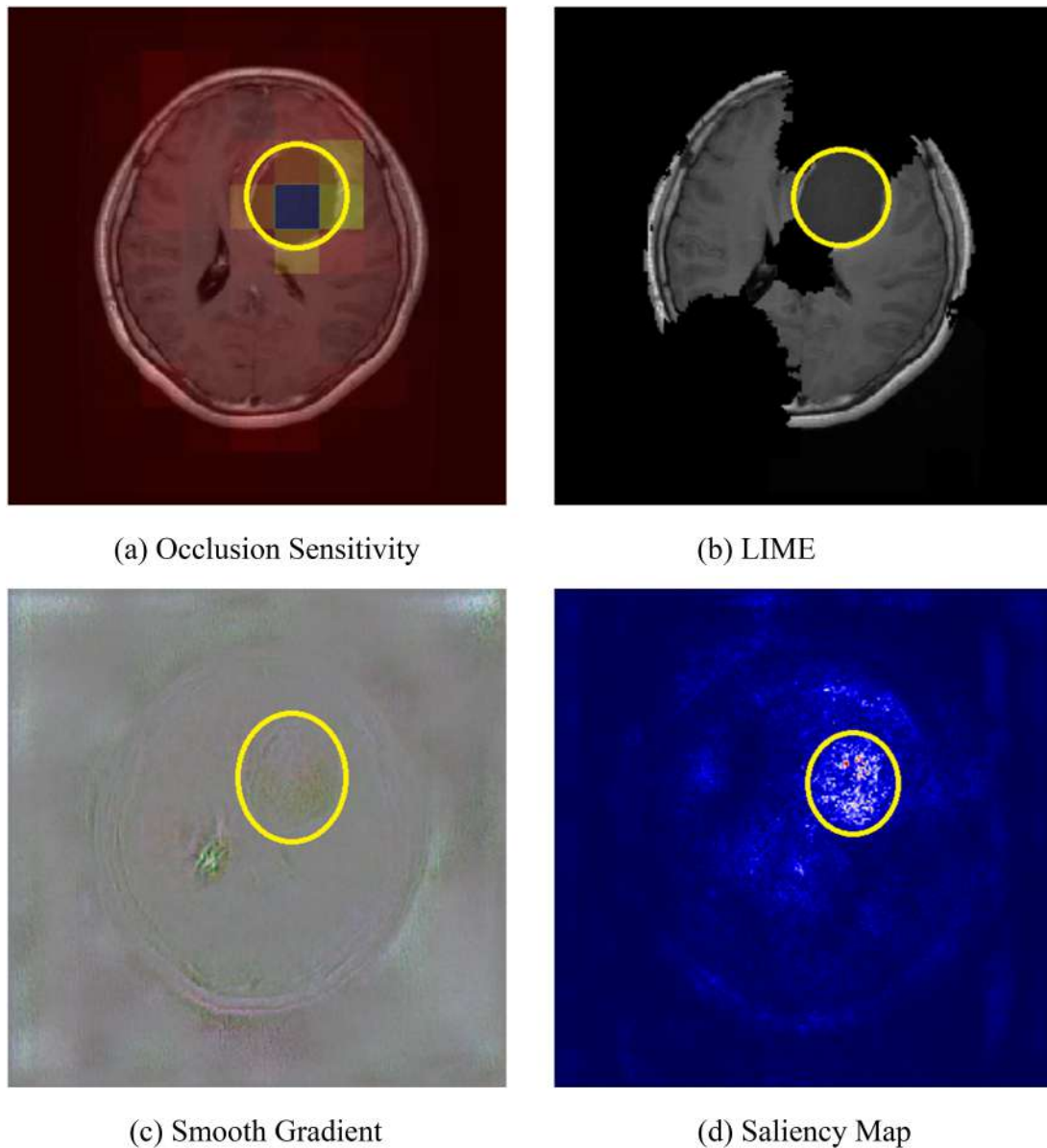
(a) Occlusion Sensitivity

(b) LIME

(c) Smooth Gradient

(d) Saliency Map

FIGURE 8 | Visualization of interpretability methods applied to glioma MRI images.

sharp activations reinforced the model's confidence in healthy predictions, and the consistency of highlighted regions across perturbations supported the reliability of Smooth Gradients in identifying relevant features, though with reduced effectiveness for pituitary tumor localization.

From Figures 8d, 9d, 10d, and 11d, saliency maps provided fine-grained pixel-level attributions that sharply delineated the boundaries of tumor regions. These maps revealed the highest activation gradients precisely aligned with the actual tumor locations in the MRI scans, suggesting that the model effectively leverages spatially relevant tumor features. The clear boundary-focused attention observed in the saliency visualizations demonstrates that BTCNet-CNN is not only sensitive to the presence of lesions but also captures their structural characteristics. The absence of high gradient activations in the no-tumor class revealed that the model's choice was based on a general lack of abnormal patterns, rather than reliance on irrelevant image regions.

4.3 | BTCNET-CNN Versus State-of-The-Art Models

BTCNet-CNN's performance was compared against several state-of-the-art models reported in the literature. As shown in Table 9, BTCNet-CNN outperformed the others with an accuracy of 99.31%, surpassing other competitive models such as Hybrid 3B Net [28], CNN + MS-DAM [29], ViT-GRU [30], XAISS-BMLBT [31], CNN-SVM [32], U-Net [33], and ResNet50 [34]. In addition to accuracy, the precision (99.25%), recall
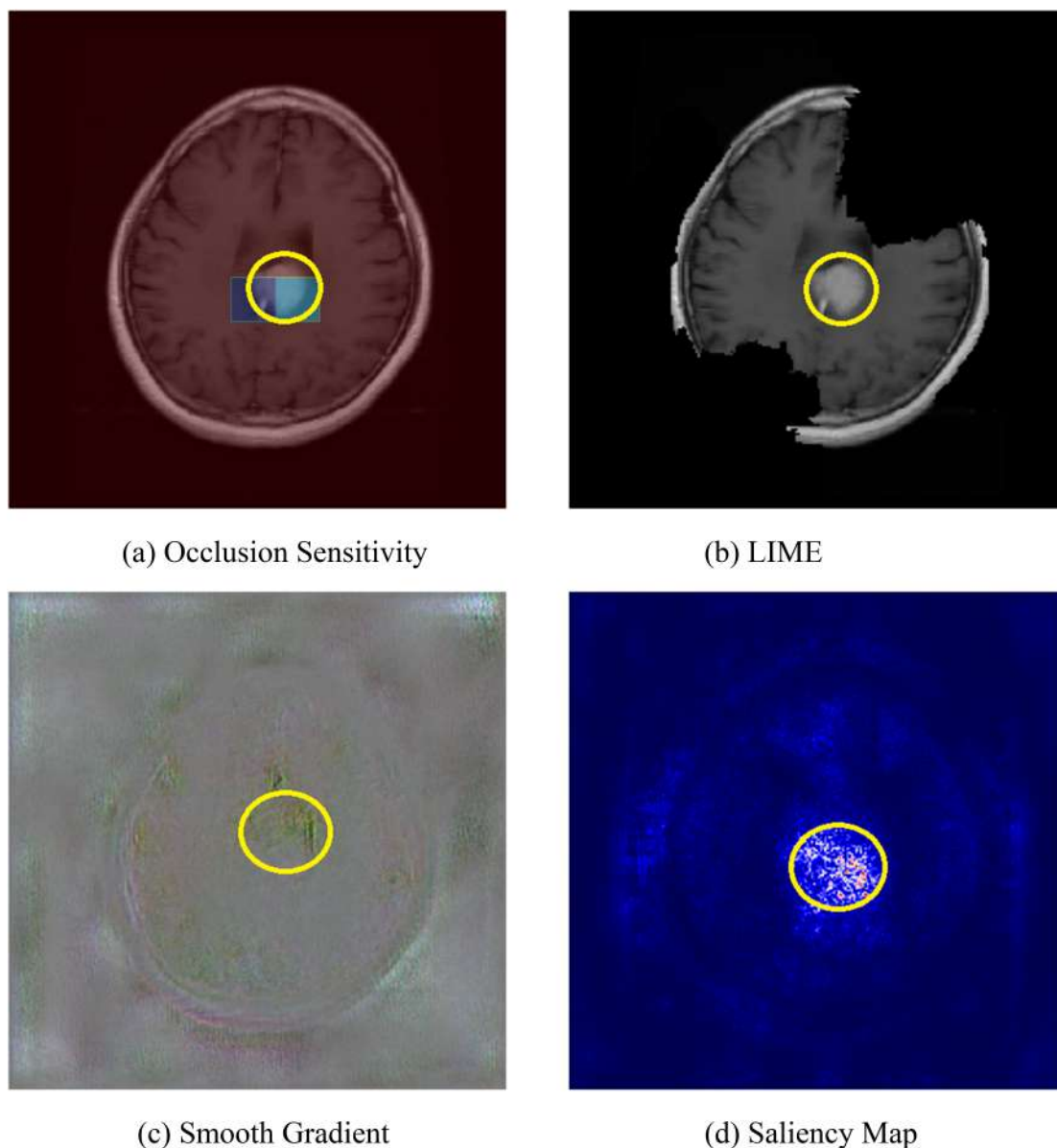
(a) Occlusion Sensitivity

(b) LIME

(c) Smooth Gradient

(d) Saliency Map

FIGURE 9 | Visualization of interpretability methods applied to Meningioma MRI images.

(99.25%), and F1 score (99.5%) of BTCNet-CNN also outperformed most of the existing methods. These values were computed as the average across the four tumor classes, ensuring a balanced evaluation. It is clear that the proposed BTCNet-CNN consistently demonstrates superior classification effectiveness and reliability for real-world BT detection applications using MRI data.

5 | Discussion and Insights

Experimental findings indicate that the proposed BTCNet-CNN surpasses both conventional transfer learning models and recent state-of-the-art architectures in terms of accuracy, generalization, and interpretability. While ResNet50 and InceptionV3 showed varying levels of competence, their performances were affected by either limited generalization (in the case of ResNet50) or

occasional class-level inconsistencies (as seen with InceptionV3). Specifically, ResNet50 exhibited the weakest performance, struggling particularly with the meningioma class, likely due to its lower capability to extract discriminative features from complex tumor morphologies. In contrast, InceptionV3's multi-scale feature extraction helped it deliver stronger results, though it still misclassified a significant number of non-tumor and meningioma samples, highlighting the inter-class similarity challenge. BTCNet-CNN not only achieved the highest training, validation, and testing accuracies but also recorded the lowest testing loss, indicating effective learning without overfitting. Its class-wise performance revealed near-perfect results across all tumor categories. Precision, recall, and F1 scores were averaged to compare the performance of BTCNet-CNN with the existing works. BTCNet-CNN achieved 99.25% precision, 99.25% recall, and 99.5% F1 score.
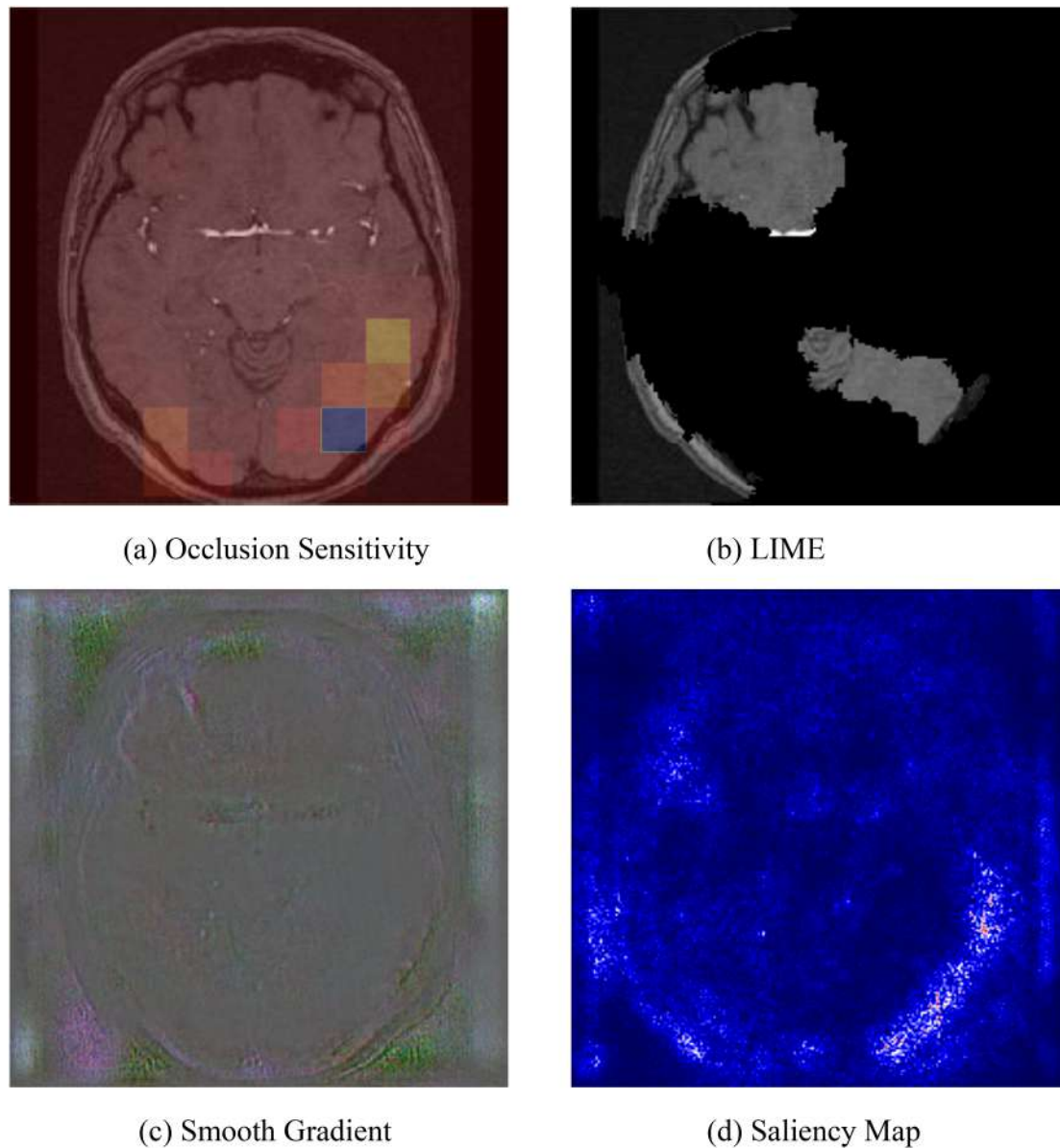
(a) Occlusion Sensitivity

(b) LIME

(c) Smooth Gradient

(d) Saliency Map

FIGURE 10 | Visualization of interpretability methods applied to an MRI scan without a tumor.

The proposed BTCNet-CNN model exhibits several merits that contribute to its superior performance and clinical applicability. First, its lightweight architecture efficiently extracts discriminative features from MRI images while maintaining a balance between model depth and computational cost, enabling faster training and inference. The use of progressively increasing convolutional filters allows hierarchical feature learning, resulting in robust tumor classification even in complex MRI scenarios. The inclusion of batch normalization, dropout, and L2 regularization significantly enhances model generalization and reduces overfitting. Additionally, a major drawback of traditional deep learning models in clinical settings is addressed by the inclusion of XAI approaches, such as Occlusion Sensitivity, LIME, Smooth Gradients, and Saliency Maps, which provide transparent and interpretable decision-making. The statistical validation using McNemar's test confirms that BTCNet-CNN outperforms state-of-the-art models statistically and not by chance.

6 | Streamlit Hosting

A web application was built using Streamlit to facilitate user interaction and real-time prediction by integrating BTCNet-CNN. The interface of the application is shown in Figure 12. With Streamlit's markdown and CSS support, the app was styled to be user-friendly and visually appealing. The header, sub-header, and prediction output are displayed using custom CSS. Users can upload medical images in JPG, JPEG, or PNG format for BT classification. Once an image is uploaded, Streamlit passes it through the BTCNet-CNN in real time and displays the predicted class and confidence level instantly. Users can interactively select different explainability methods (Occlusion Sensitivity, LIME, Smooth
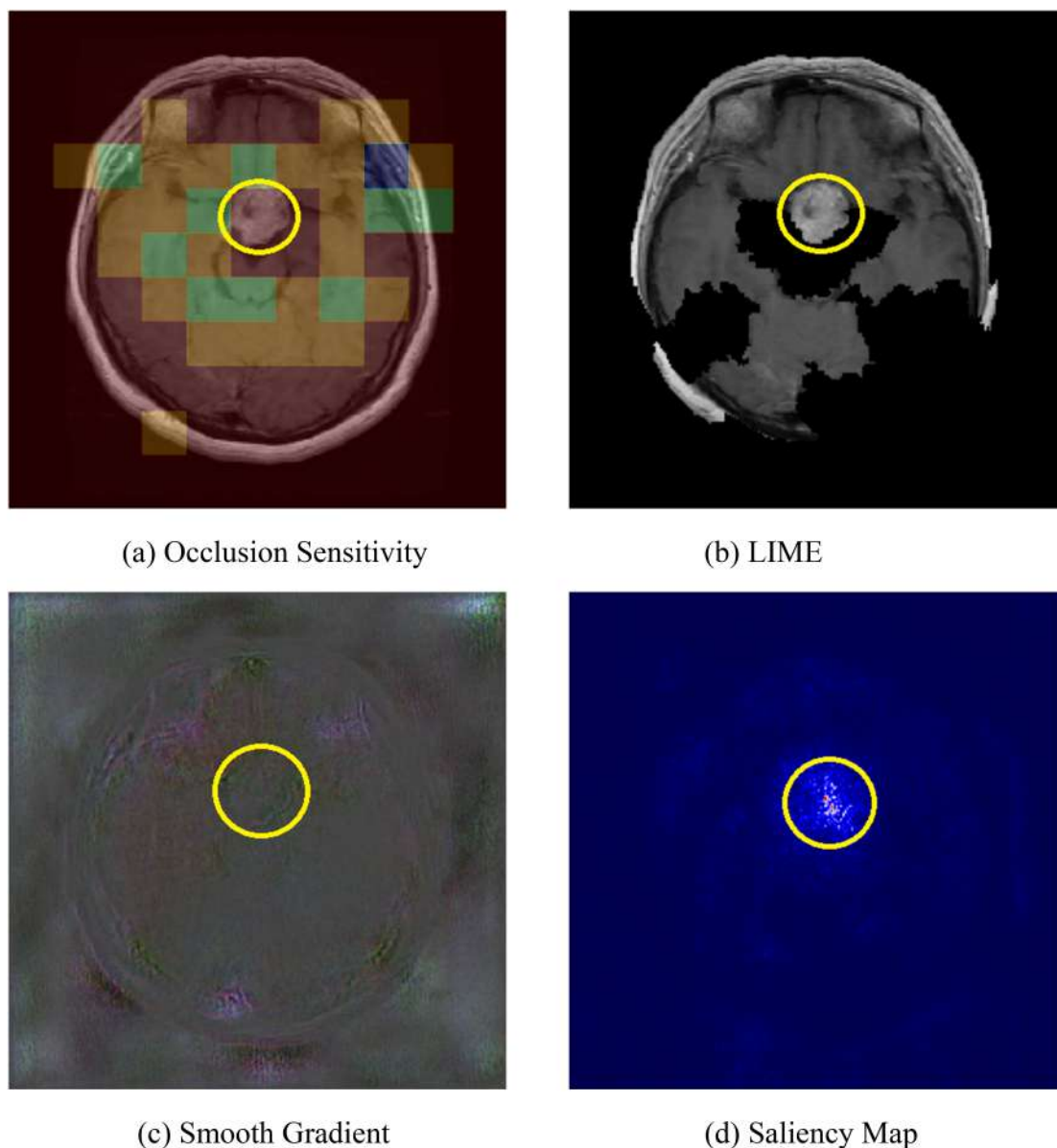
(a) Occlusion Sensitivity

(b) LIME

(c) Smooth Gradient

(d) Saliency Map

FIGURE 11 | Visualization of interpretability methods applied to pituitary tumor MRI images.

Gradients, Saliency Map) through radio buttons, and generate insightful visualizations with just one click. Probabilities are visualized using dynamic bar charts, and prediction confidence is shown with a progress bar. TensorFlow models and XAI techniques are integrated smoothly with the Streamlit front end, offering a complete end-to-end solution from image upload to visual explanation.
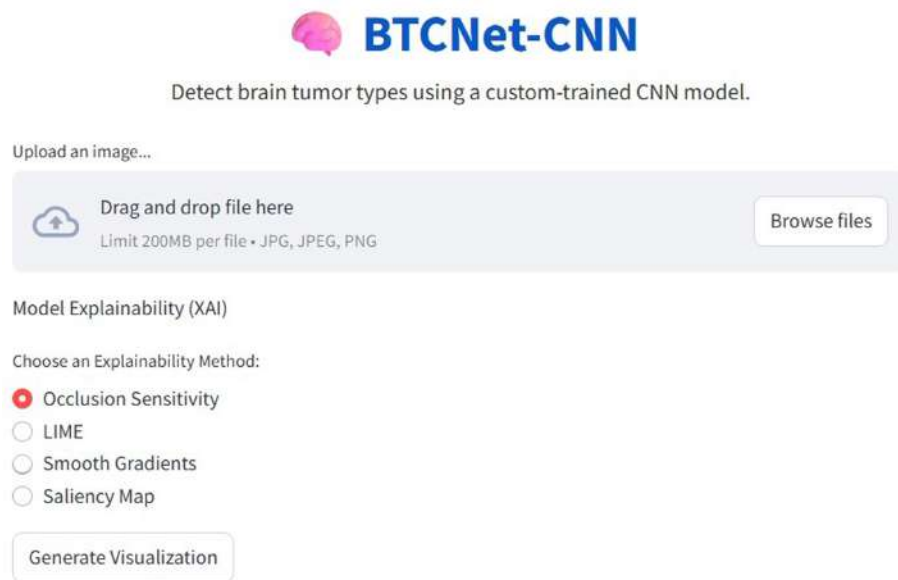
7 | Conclusions

This research proposed and evaluated a new deep learning architecture, BTCNet-CNN, for the multi-class classification of BT using MRI images. Through comparative experimentation with ResNet50 and InceptionV3, BTCNet-CNN outperformed across all evaluation metrics. It achieved an accuracy of 99.31% and a loss of 0.118 on the unseen data. The class-wise precision of more than 98%, recall of more than 97%, and F1 scores of more than 99% indicate the classification power of the BTCNet-CNN. Furthermore, using XAI techniques showed the reliability of BTCNet-CNN's predictions. The XAI visualizations confirmed that the model consistently focused on tumor-specific regions in MRI scans, reinforcing the reliability of its predictions. Despite its strong performance, BTCNet-CNN has a few limitations. It was evaluated on a single publicly available dataset, which may not fully represent the variability encountered in real-world clinical settings. One area that can improve this research is incorporating a larger dataset with images from multiple regions of the world, which enhances the generalization power across different tumor variations. The model could also be extended to 3D volumetric analysis using 3D CNNs to leverage the full spatial context of brain scans. Future work could include incorporating

TABLE 9 | Comparison of BTCNet-CNN and state-of-the-art models.

Refs.	Model	Accuracy (%)	Precision (%)	Recall (%)	F1 Score (%)
[28]	Hybrid 3B Net	97.01	97.03	97.01	97.01
[29]	CNN + MS-DAM	96.61	95.67	97.22	96.43
[30]	ViT-GRU	98.97	97	97	97
[31]	XAISS-BMLBT	97.75	95.56	95.42	95.48
[32]	CNN-SVM	99	97.3	—	—
[33]	U-Net	96.01	96	96	96
[34]	ResNet50	98.52	98.5	98	98
[35]	BTR-EODLA	98.78	98.12	98.78	98.43
Proposed	BTCNet-CNN	99.31	99.25	99.25	99.5

FIGURE 12 | Streamlit application interface.

a lightweight, efficient attention-based mechanism for enhanced feature extraction. Another promising direction is integrating multimodal data, such as genetic markers, clinical reports, or PET scans, alongside MRI, to enable a more holistic diagnosis. Further, real-time deployment via mobile or cloud-based platforms could be explored to facilitate AI-assisted diagnostics in low-resource or rural healthcare settings.

Author Contributions

Duppala Rohan: conceptualization, writing – original draft, investigation. **Boddepalli Yaswanth:** data curation, investigation, writing – original draft, methodology. **V. S. Sai Vardhan:** formal analysis, writing – original draft, conceptualization. **G. Pradeep Reddy:** methodology, project administration, writing – review and editing, data curation. **K. Purna Prakash:** validation, visualization, writing – review and editing, investigation. **Y. V. Pavan Kumar:** methodology, supervision, writing – review and editing, resources, funding acquisition, software.

Conflicts of Interest

The authors declare no conflicts of interest.

Data Availability Statement

The data that support the findings of this study are openly available in Brain Tumor MRIs at https://www.kaggle.com/datasets/vinayjayanti/brain-tumor-mris.

References

1. G. Osborn, D. N. Louis, T. Y. Poussaint, L. L. Linscott, and K. L. Salzman, "The 2021 World Health Organization Classification of Tumors of the Central Nervous System: What Neuroradiologists Need to Know," *American Journal of Neuroradiology* 43, no. 7 (2022): 928–937, https://doi.org/10.3174/ajnr.A7462.

2. G. Pradeep Reddy, D. Rohan, Y. V. P. Kumar, K. P. Prakash, and M. Srikanth, "Artificial Intelligence-Based Effective Detection of Parkinson's Disease Using Voice Measurements," *Engineering Proceedings* 82, no. 1 (2024): 28, https://doi.org/10.3390/ecsa-11-20481.

3. G. Pradeep Reddy, D. Rohan, S. M. A. Kareem, Y. Venkata Pavan Kumar, K. Purna Prakash, and M. Janapati, "A Custom Convolutional Neural Network Model-Based Bioimaging Technique for Enhanced Accuracy of Alzheimer's Disease Detection," *Engineering Proceedings* 87, no. 1 (2025): 47, https://doi.org/10.3390/engproc2025087047.

4. D. Rohan, G. P. Reddy, Y. V. P. Kumar, K. P. Prakash, and C. P. Reddy, "An Extensive Experimental Analysis for Heart Disease Prediction Using

Artificial Intelligence Techniques," *Scientific Reports* 15, no. 1 (2025): 6132, https://doi.org/10.1038/s41598-025-90530-1.

5. G. P. Reddy and Y. V. P. Kumar, "Explainable AI (XAI): Explained," in 2023 IEEE Open Conference of Electrical, Electronic and Information Sciences (eStream), Vilnius, Lithuania: IEEE, Apr. 2023, pp. 1–6, https://doi.org/10.1109/eStream59056.2023.10134984.

6. S. Iftikhar, N. Anjum, A. B. Siddiqui, M. Ur Rehman, and N. Ramzan, "Explainable CNN for Brain Tumor Detection and Classification Through XAI Based Key Features Identification," *Brain Informatics* 12, no. 1 (2025): 10, https://doi.org/10.1186/s40708-025-00257-y.

7. S. Benfatto, M. Sill, D. T. W. Jones, et al., "Explainable Artificial Intelligence of DNA Methylation-Based Brain Tumor Diagnostics," *Nature Communications* 16, no. 1 (2025): 1787, https://doi.org/10.1038/s41467-025-57078-0.

8. K. Lamba, S. Rani, and M. Shabaz, "Synergizing Advanced Algorithm of Explainable Artificial Intelligence With Hybrid Model for Enhanced Brain Tumor Detection in Healthcare," *Scientific Reports* 15, no. 1 (2025): 20489, https://doi.org/10.1038/s41598-025-07524-2.

9. R. Preetha, M. J. P. Priyadarsini, and J. S. Nisha, "Brain Tumor Segmentation Using Multi-Scale Attention U-Net With EfficientNetB4 Encoder for Enhanced MRI Analysis," *Scientific Reports* 15, no. 1 (2025): 9914, https://doi.org/10.1038/s41598-025-94267-9.

10. M. Ariful Islam, M. F. Mridha, M. Safran, S. Alfarhood, and M. Mohsin Kabir, "Revolutionizing Brain Tumor Detection Using Explainable AI in MRI Images," *NMR in Biomedicine* 38, no. 3 (2025): e70001, https://doi.org/10.1002/nbm.70001.

11. Q. Mastoi, S. Latif, S. Brohi, et al., "Explainable AI in Medical Imaging: An Interpretable and Collaborative Federated Learning Model for Brain Tumor Classification," *Frontiers in Oncology* 15 (2025): 1535478, https://doi.org/10.3389/fonc.2025.1535478.

12. S. K. Mathivanan, S. Srinivasan, M. S. Koti, V. S. Kushwah, R. B. Joseph, and M. A. Shah, "A Secure Hybrid Deep Learning Framework for Brain Tumor Detection and Classification," *Journal of Big Data* 12, no. 1 (2025): 72, https://doi.org/10.1186/s40537-025-01117-6.

13. G. Murugesan, P. Nagendran, and J. Natarajan, "Advancing Brain Tumor Diagnosis: Deep Siamese Convolutional Neural Network as a Superior Model for MRI Classification," *Brain-X* 3, no. 2 (2025): e70028, https://doi.org/10.1002/brx2.70028.

14. Y. Kaya, E. Akat, and S. Yıldırım, "Fusion-Brain-Net: A Novel Deep Fusion Model for Brain Tumor Classification," *Brain and Behavior* 15, no. 5 (2025): e70520, https://doi.org/10.1002/brb3.70520.

15. E. Gürsoy and Y. Kaya, "Brain-GCN-Net: Graph-Convolutional Neural Network for Brain Tumor Identification," *Computers in Biology and Medicine* 180 (2024): 108971, https://doi.org/10.1016/j.compbiomed.2024.108971.

16. S. U. R. Khan, M. Zhao, S. Asif, and X. Chen, "Hybrid-NET: A Fusion of DenseNet169 and Advanced Machine Learning Classifiers for Enhanced Brain Tumor Diagnosis," *International Journal of Imaging Systems and Technology* 34, no. 1 (2024): e22975, https://doi.org/10.1002/ima.22975.

17. M. I. Nazir, A. Akter, M. A. Hussen Wadud, and M. A. Uddin, "Utilizing Customized CNN for Brain Tumor Prediction With Explainable AI," *Heliyon* 10, no. 20 (2024): e38997, https://doi.org/10.1016/j.heliyon.2024.e38997.

18. Y. Mehmood and U. I. Bajwa, "Brain Tumor Grade Classification Using the ConvNext Architecture," *DIGITAL HEALTH* 10 (2024): 20552076241284920, https://doi.org/10.1177/20552076241284920.

19. R. Haque, M. M. Hassan, A. K. Bairagi, and S. M. Shariful Islam, "NeuroNet19: An Explainable Deep Neural Network Model for the Classification of Brain Tumors Using Magnetic Resonance Imaging Data," *Scientific Reports* 14, no. 1 (2024): 1524, https://doi.org/10.1038/s41598-024-51867-1.

20. R. A. Zeineldin, M. E. Karar, Z. Elshaer, et al., "Explainable Hybrid Vision Transformers and Convolutional Network for Multimodal Glioma Segmentation in Brain MRI," *Scientific Reports* 14, no. 1 (2024): 3713, https://doi.org/10.1038/s41598-024-54186-7.

21. F. Yan, Y. Chen, Y. Xia, Z. Wang, and R. Xiao, "An Explainable Brain Tumor Detection Framework for MRI Analysis," *Applied Sciences* 13, no. 6 (2023): 3438, https://doi.org/10.3390/app13063438.

22. V. Jayanti, "Brain Tumor MRIs. Kaggle", https://doi.org/10.34740/KAGGLE/DSV/6758053.

23. P. H. V. Valois, K. Niinuma, and K. Fukui, "Occlusion Sensitivity Analysis with Augmentation Subspace Perturbation in Deep Feature Space," in 2024 IEEE/CVF Winter Conference on Applications of Computer Vision (WACV), Waikoloa, HI, USA: IEEE, Jan. 2024, pp. 4817–4826, https://doi.org/10.1109/WACV57701.2024.00476.

24. M. T. Ribeiro, S. Singh, and C. Guestrin, "'Why Should I Trust You?': Explaining the Predictions of Any Classifier," in Proceedings of the 22nd ACM SIGKDD International Conference on Knowledge Discovery and Data Mining, San Francisco, California, USA: ACM, Aug. 2016, pp. 1135–1144, https://doi.org/10.1145/2939672.2939778.

25. D. Smilkov, N. Thorat, B. Kim, F. Viégas, and M. Wattenberg, "SmoothGrad: Removing Noise by Adding Noise," 2017, arXiv, https://doi.org/10.48550/ARXIV.1706.03825.

26. T. N. Mundhenk, B. Y. Chen, and G. Friedland, "Efficient Saliency Maps for Explainable AI," 2019, arXiv, https://doi.org/10.48550/ARXIV.1911.11293.

27. B. Şener, K. Acici, and E. Sümer, "Categorization of Alzheimer's Disease Stages Using Deep Learning Approaches With Mcnemar's Test," *PeerJ Computer Science* 10 (2024): e1877, https://doi.org/10.7717/peerj-cs.1877.

28. R. Preetha, M. J. P. Priyadarsini, and J. S. Nisha, "Hybrid 3B Net and EfficientNetB2 Model for Multi-Class Brain Tumor Classification," *IEEE Access* 13 (2025): 63465–63485, https://doi.org/10.1109/ACCESS.2025.3558411.

29. E. Zarenia, A. A. Far, and K. Rezaee, "Automated Multi-Class MRI Brain Tumor Classification and Segmentation Using Deformable Attention and Saliency Mapping," *Scientific Reports* 15, no. 1 (2025): 8114, https://doi.org/10.1038/s41598-025-92776-1.

30. M. M. Ahmed, M. M. Hossain, M. R. Islam, et al., "Brain Tumor Detection and Classification in MRI Using Hybrid ViT and GRU Model With Explainable AI in Southern Bangladesh," *Scientific Reports* 14, no. 1 (2024): 22797, https://doi.org/10.1038/s41598-024-71893-3.

31. K. Lakshmi, S. Amaran, G. Subbulakshmi, S. Padmini, G. P. Joshi, and W. Cho, "Explainable Artificial Intelligence With UNet Based Segmentation and Bayesian Machine Learning for Classification of Brain Tumors Using MRI Images," *Scientific Reports* 15, no. 1 (2025): 690, https://doi.org/10.1038/s41598-024-84692-7.

32. C. Gunasundari and K. Selva Bhuvaneswari, "A Novel Approach for the Detection of Brain Tumor and Its Classification via Independent Component Analysis," *Scientific Reports* 15, no. 1 (2025): 8252, https://doi.org/10.1038/s41598-025-87934-4.

33. M. A. Ilani, D. Shi, and Y. M. Banad, "T1-Weighted MRI-Based Brain Tumor Classification Using Hybrid Deep Learning Models," *Scientific Reports* 15, no. 1 (2025): 7010, https://doi.org/10.1038/s41598-025-92020-w.

34. M. M. Mohamed, T. R. Mahesh, V. K. Vinoth, and S. Guluwadi, "Enhancing Brain Tumor Detection in MRI Images Through Explainable AI Using Grad-CAM With Resnet 50," *BMC Medical Imaging* 24, no. 1 (2024): 107, https://doi.org/10.1186/s12880-024-01292-7.

35. M. Ragab, I. Katib, S. A. Sharaf, et al., "Automated Brain Tumor Recognition Using Equilibrium Optimizer With Deep Learning Approach on MRI Images," *Scientific Reports* 14, no. 1 (2024): 29448, https://doi.org/10.1038/s41598-024-80888-z.